scientific reports

OPEN

Multiscale mushy layer model for Arctic marginal ice zone dynamics

Courtenay Strong[1]✉, Elena Cherkaev[2] & Kenneth M. Golden[2]

Perhaps the most dynamic component of the Arctic sea ice cover is the marginal ice zone (MIZ), the transitional region between dense pack ice to the north and open ocean to the south. It widens by a factor of four while seasonally migrating more than 1600 km poleward in the Bering–Chukchi Sea sector, impacting climate dynamics, ecological processes, and human accessibility to the Arctic. Here we showcase a transformative mathematical modeling approach to understanding changes in MIZ location and width, focusing on their seasonal cycles as observed by satellites. We view the MIZ as a liquid-solid phase transition region, or mushy zone, on the scale of the Arctic Ocean. Invoking the physics of phase changes, the MIZ is modeled as a dynamic, multiscale composite material layer; this model captures 96% of the annual cycle of MIZ location and 78% of the annual cycle of MIZ width. Temperature in the upper ocean is described by a nonlinear heat equation with effective parameters obtained using homogenization theory for a random medium of ice floes in a sea water host. Observations and simulations together indicate that MIZ location closely tracks the below-ice 273 K isotherm while the width of the MIZ follows vertical heat flux convergence, but with a three-week lag.

Summer Arctic sea ice extent, age, and thickness have been declining at an accelerating pace over the past few decades, and the amplitude of the seasonal cycle has abruptly increased[1–4]. These changes in the Arctic sea ice cover are accompanied by changes in the geometry of the marginal ice zone (MIZ), which is the dynamic and biologically active transition region between dense inner pack ice to the north and open ocean to the south[5–9]. MIZ width has increased by 40% over the satellite era[9–13], impacting atmosphere-ocean energy exchange[14], polar ecosystem dynamics and habitat selection[15–19], navigability of the Arctic for humans[20–22], and the penetration of waves into the ice cover which affects melting, freezing, and floe-breaking processes[23]. Broad interest in the MIZ underscores the need to understand the basic physics of its evolution and trends[24]. Fully coupled global climate models can reasonably capture aspects of MIZ variability over the sea ice annual cycle[25], but the complexity of these models makes it challenging to understand the basic physical processes, from the small scale up, at work in determining MIZ dynamics.

The upper layer of the Arctic Ocean with sea ice can be thought of as a two-phase (solid and liquid), two-component (sea ice and sea water) granular composite. The interacting grains or particles range in size over many orders of magnitude, and the system exhibits rich dynamics on oceanic scales in response to mechanical and thermodynamic forcing. Modeling this macroscopic behavior is similar to statistical mechanics, which can describe complex collective behavior such as phase transitions, transport processes, and response to forcing for systems with a large number of particles or degrees of freedom. While statistical physics has seen wide-spread success in similar problems in other fields, it has been applied to the physics of sea ice in only a few contexts[26]. This study advances the vision[26] of bringing ideas and methods of statistical physics and phase transitions to bear on sea ice science.

Our main innovation here is to consider the MIZ as a macroscale phase change front, drawing on the physics of moving boundary problems[27]. The melting fronts in this problem are conventionally thought of as being much smaller-scale than the MIZ itself, residing where lateral melting occurs on individual floes and basal melting occurs at the bottom interface with sea water. However, at the larger pan-Arctic spatial scales considered here, the upper ocean layer is thought of as a composite of ice floes in a sea water host, with the MIZ being a finite-width phase transition region separating the "solid" core of dense Arctic pack ice to the north from the "liquid" ocean phase to the south. It is now widely recognized that melting fronts are often transition zones rather than sharp discontinuities in phase. These effects are often difficult to deal with analytically, but insights have been gained via numerical investigation[28,29]. Even in pure substances with a defined melting temperature, "mushy" regions or

[1]Department of Atmospheric Sciences, University of Utah, Salt Lake City, UT, USA. [2]Department of Mathematics, University of Utah, Salt Lake City, UT, USA. ✉email: court.strong@utah.edu

layers can occur where solid and liquid phases coexist near the melting temperature[30]. We propose a multiscale mushy layer model to interpret the seasonality in width and location of the MIZ observed by satellites. We note that this task cannot be performed directly from an ocean reanalysis dataset, such as GLORYS2V4, because while solving a set of large-scale coupled equations, its underlying model employs data assimilation.

For ocean processes involving phase changes in a water-salt-ice mixture, there is theoretical and empirical support for the existence of a finite-width phase transition zone[31]. Sea ice itself is a two-phase (solid and liquid), two-component (ice and brine) system which can be modeled by the mathematics and physics of mushy layers[32–36]. Here we adapt these powerful ideas to large scale sea ice dynamics, and consider the MIZ to be an ocean-scale mushy layer separating the solid phase to the north from the liquid phase to the south. Furthermore, we employ methods of homogenization, inspired by computations in statistical mechanics, to find the large-scale effective parameters of the ice cover that enter into our MIZ model, based on smaller scale information such as sea ice concentration and floe geometry.

Results

Observed MIZ

The MIZ is defined as the region where sea ice concentration (SIC) ranges between SIC = 0.15 and SIC = 0.8 as in our prior work[10,11,37]. Representative examples of the analyzed MIZ are shown in Fig. 1. We focus here on the Bering–Chukchi Sea sector because it features the most dramatic MIZ seasonal cycles observed in the Arctic (e.g., Fig. 1). As sea ice extent maximizes during spring and pack ice extends into the Bering Strait, the MIZ location (central latitude, denoted s) of the Bering–Chukchi Sea MIZ minimizes close to 60°N (Fig. 2a,b). At the other extreme, sea ice extent minimizes during fall and the MIZ migrates more than 1600 km poleward to around 75°N before returning south by the end of the calendar year (Fig. 2a,b). This migration closely follows the latitude at which $T_b = 273$ K, where T_b is the below-ice sea water temperature at depth $z_b = -5$ m in the GLORYS2V4 Reanalysis. Denoting this latitude by $\phi(T_b = 273\text{ K})$, the squared Pearson correlation $r^2[s, \phi(T_b = 273\text{ K})] = 0.97$ indicates that migration of the 273-K isotherm accounts for 97% of the MIZ location seasonal cycle.

MIZ width w fluctuates around 75 km for most of the year, but dramatically increases by a factor of four during days of year 175–225, and then returns back to around 75 km by day of year 275 (Fig. 2c). This annual cycle of w has a strong lagged correlation with the difference between the below-ice temperature and skin temperature evaluated at the MIZ location, denoted $(T_b - T_0)|_{\phi=s}$, where skin temperature (T_0) refers to the temperature of the very thin surface layer of the ocean or sea ice, which directly interacts with the atmosphere[38]. A 100-day pulse of strong positive $(T_b - T_0)|_{\phi=s}$ leads the MIZ widening cycle by three weeks (dotted red curves, Fig. 2d) yielding a 21-day lagged correlation $r^2[w, (T_b - T_0)|_{\phi=s}]$=0.92. On the physical mechanism underlying this strong lagged correlation, $(T_b - T_0)|_{\phi=s}$ is proportional to vertical heat flux ($J_z = -k_z \partial T/\partial z$) averaged over the depth of the sea water-sea ice layer. Such averaging results in the vertical component k_z of the effective thermal conductivity tensor $\mathbf{k}$ of this layer

$$\frac{1}{|z_b|}\int_{z_b}^{0} J_z \, \mathrm{dz} = \frac{\mathrm{k_z}}{|\mathrm{z_b}|}(\mathrm{T_b} - \mathrm{T_0}). \tag{1}$$

The 100-day pulse of strong positive temperature difference $(T_b - T_0)|_{\phi=s}$ is thus a physically plausible driver of the MIZ widening cycle, with the three-week lag interpreted as the time scale for required thinning of the sea ice.

Macroscale moving boundary model

Results given above based on analysis of satellite-derived sea ice concentrations and ocean reanalyses indicate that the drivers of MIZ width and location are visible in temperatures at the surface and below the ice at depth z_b. A suitable thermodynamic model forced by these boundary conditions might thus be able to capture the observed MIZ seasonal cycles. The success of such a model increases our confidence in the causal mechanisms theorized above and provides an opportunity to gain further insight into the MIZ through analysis of the model solution.

Our approach is to model the MIZ as the solution of a macroscale phase transition problem. We consider the uppermost layer of the ocean as a two-phase composite of sea ice and sea water[36,39]. Using ideas from moving boundary problems and simulation of phase change fronts[27,29,40], we model temperature T in this layer using a heat equation with a nonlinear source term which governs the evolution of latent heat

$$\rho c \frac{\partial T}{\partial t} = \nabla \cdot (\mathbf{k}\nabla T) + \delta H \frac{\partial \psi}{\partial t}. \tag{2}$$

Here ψ is the volume fraction of ice, ρ and c are the effective density and specific heat, respectively, calculated as concentration-weighted averages, and

$$\delta H = \rho(c_l - c_s)T + \rho L \tag{3}$$

is the difference between liquid and solid enthalpies corresponding to a reference temperature of zero Kelvin with L being the latent heat of fusion[40]. The effective parameter $\mathbf{k}$ is generally an anisotropic tensor which accounts for the thermal conductivity of the sea ice solid phase of the composite as well as for turbulent thermal transport in the liquid phase[41–45]. To reduce the model to one dependent variable, we write concentration ψ as a function of temperature using a power law formulation[46]

$$\psi = f(T) = 1 - \left(\frac{T - T_s}{T_l - T_s}\right)^{\alpha}. \tag{4}$$

Notation	Value	Name
ρ_s	900 kg m^{-3}	Density of sea ice[48]
ρ_l	1025 kg m^{-3}	Density of sea water[48]
c_s	2.1 kJ kg^{-1}K^{-1}	Specific heat capacity of sea ice[48]
c_l	4.0 kJ kg^{-1}K^{-1}	Specific heat capacity of sea water[78]
k_s	2.2 W m^{-1}K^{-1}	Thermal conductivity of sea ice[48]
D_T	5×10^{-6}m^{2}s^{-1}	Thermal diffusivity of sea water[79]
k_l	20.5 W m^{-1}K^{-1}	Effective thermal conductivity of sea water
T_l	271.90 K	Threshold for fully liquid state
T_s	271.35 K	Threshold for fully solid state
α	0.8	Exponent in equation (4)

Table 1. Model parameters.

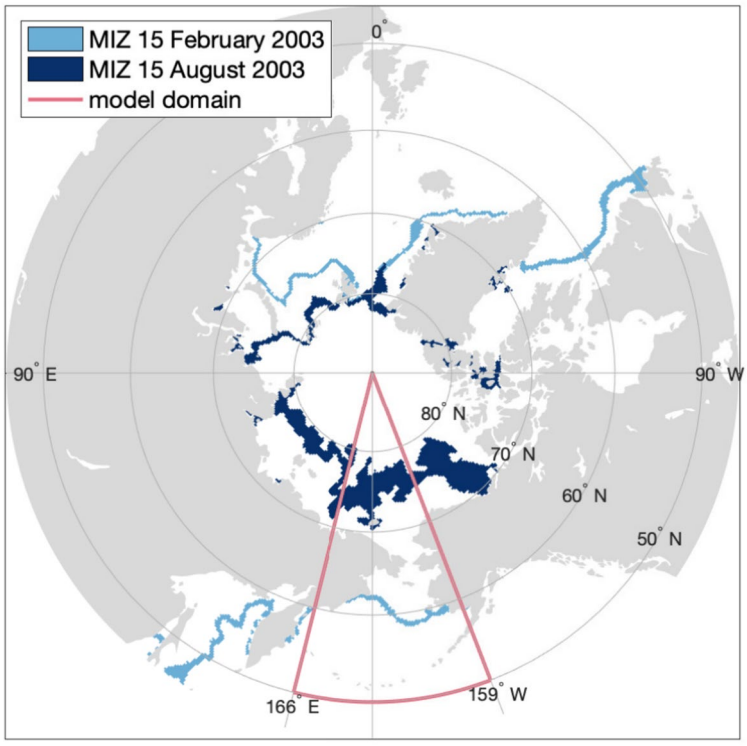

Figure 1. Marginal ice zone. Illustrative MIZ configurations from 15 February 2003 (light blue shading) and 15 August 2003 (dark blue shading). The simulation domain is the Bering–Chukchi Sea sector is outlined in red (166°E and 159°W).

Here T_s = 271.35K was prescribed to correspond to the fully solid condition, and the two free parameters $\alpha = 0.8$ and T_l = 271.9K were chosen to achieve a realistic seasonal cycle of MIZ properties and sea ice thickness (see Methods and Table 1). A simple rule was implemented to allow ice to float when one or more surface grid cells were fully liquid ($\psi = 0$) with ice ($\psi > 0$) in the underlying ice grid cell(s) (see Methods). The model is run on a two-dimensional depth-latitude domain with boundary conditions based on reanalysis data averaged with respect to longitude over the Bering–Chukchi Sea region outlined in red in Fig. 1.

Simulated MIZ

Results of numerical simulations show that the proposed model (2) produced convincing MIZ annual cycles similar to those observed by satellites, with extents and volumes being generally larger in spring than fall (Fig. 3a). The motion of the sea ice edge was realistic, with simulated MIZ location ($\hat{s}$; filled magenta circles, Fig. 3a) correlating very well with observed values, $r^2(\hat{s}, s) = 0.96$ (Fig. 3a,b). The model slightly underestimated the amplitude of the observed annual cycle of MIZ location, but captured the timing of its extrema well. Simulated

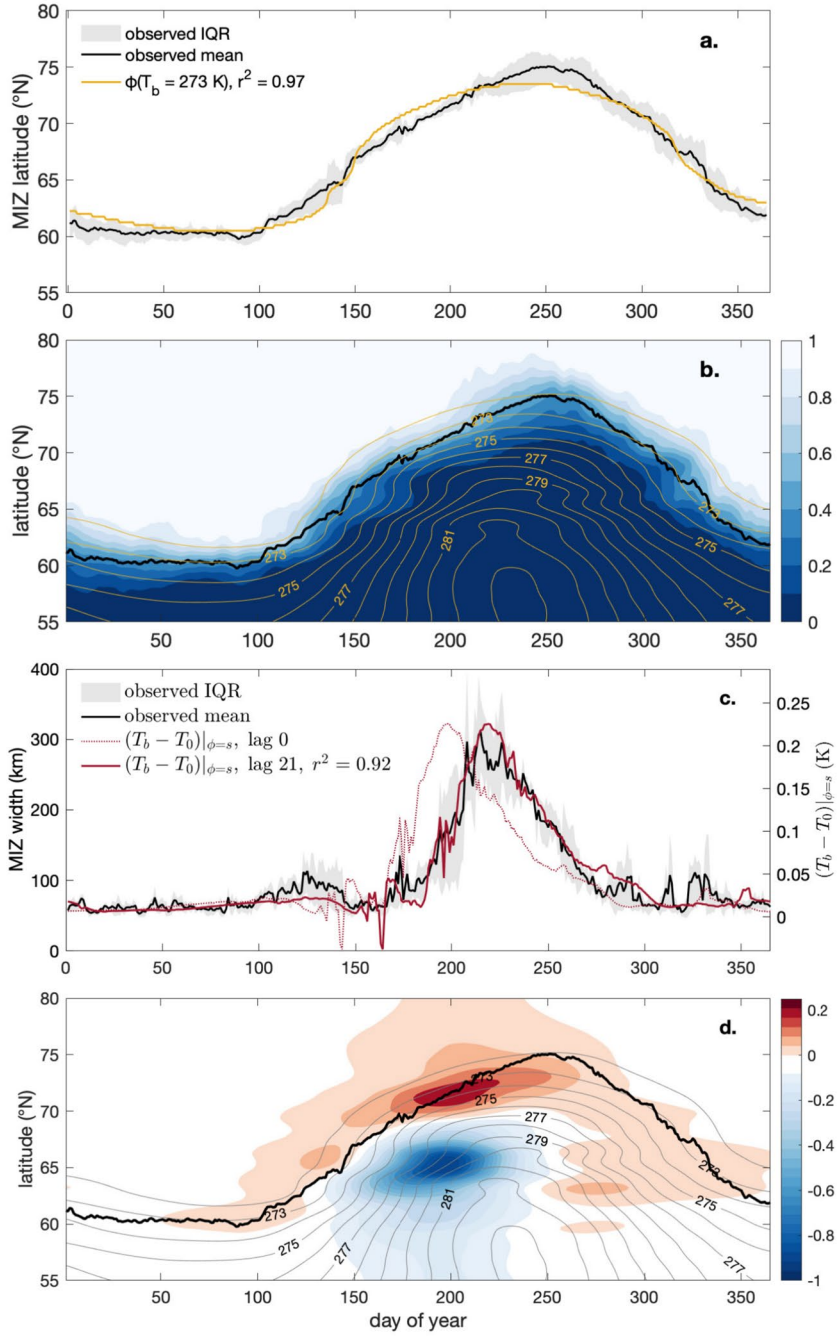

Figure 2. Observed MIZ location. For observations in the Bering–Chukchi Sea sector over the period 2000-2004: (**a**) daily mean MIZ latitude (black curve), interquartile range of daily MIZ latitude (IQR, gray shading), and daily mean latitude of the 273 K isotherm at depth 5.14 m in the GLORYS2V4 [$\phi(T_b = 273$ K), red curve]. (**b**) Observed sea ice concentration from Climate Data Record (shading), mean MIZ latitude (black curve), and 5.14-m sea water temperature from GLORYS2V4 (T_b; yellow contours, K). (**c**) daily mean MIZ width (black curve) and interquartile range (IQR) of daily MIZ width (gray shading). $(T_b - T_0)|_{\phi=s}$ denotes the below-ice temperature minus the skin temperature at the MIZ location, and is shown at zero lag (dashed red curve) and shifted to the right by 21 days (solid red curve). (**d**) $T_b - T_0$ (shading), mean MIZ latitude (black curve), and T_b (gray contours, K).

MIZ width ($\hat{w}$; magenta whiskers, Fig. 3a) underwent a widening cycle aligned with observations, yielding $r^2(\hat{w}, w) = 0.78$ (Fig. 3d).

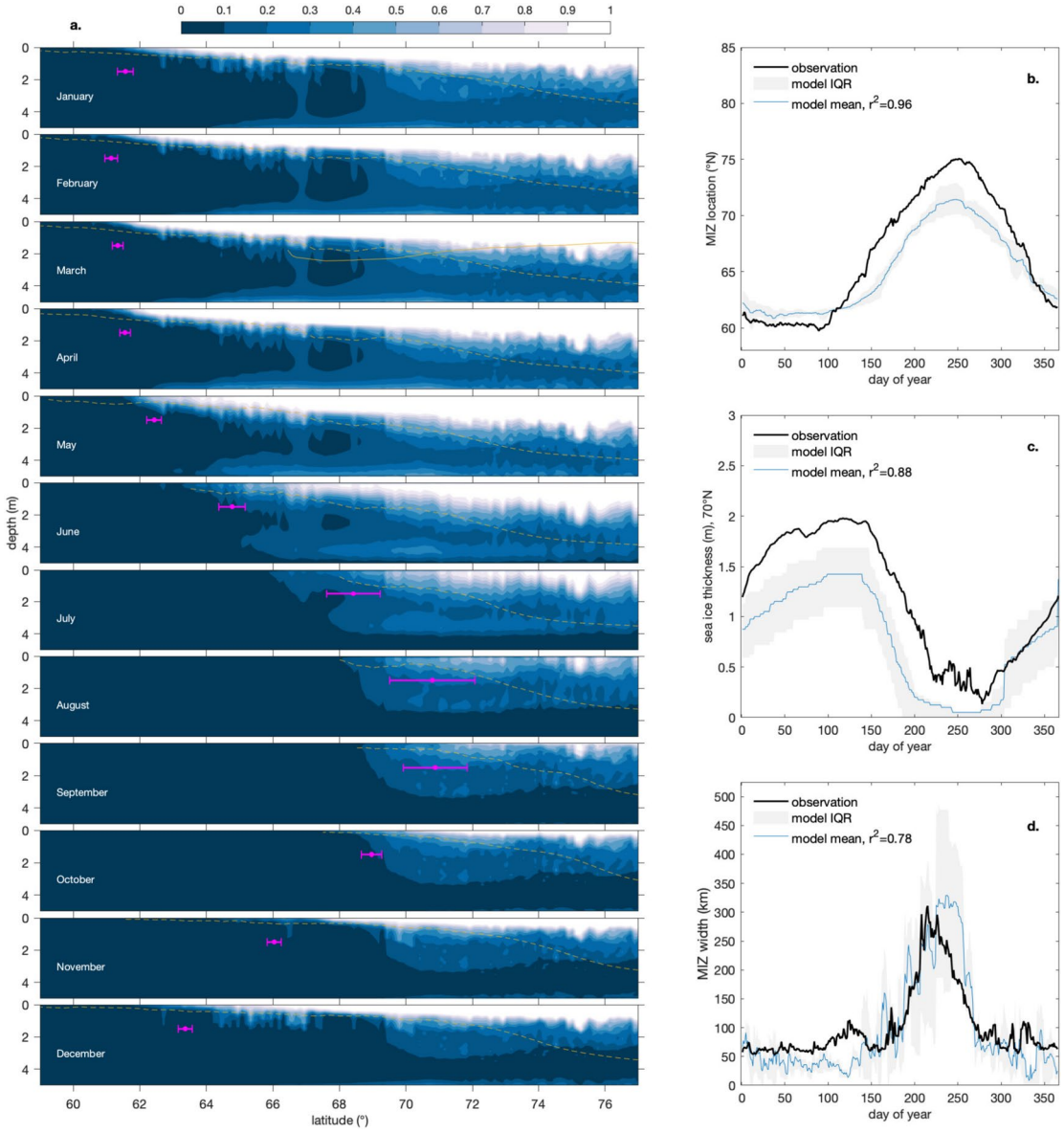

Figure 3. MIZ model. (**a**) Simulated volume fraction of ice (ψ) averaged by month over years 2000–2004. Magenta circles and whiskers indicate the MIZ location and width, respectively, both diagnosed from the model output. Dashed yellow curves are corresponding sea ice thicknesses from GLORYS2V4, and the solid yellow curve on the March panel is sea ice thickness from ICESAT for spring 2004. (**b**) Mean observed MIZ location (black curve), interquartile range of simulated MIZ location (IQR, gray shading), and mean simulated MIZ location (blue curve). (**c**) Mean sea ice thickness from GLORYS2V4 (black curve), IQR of simulated thickness of dense sea ice ($\psi > 0.8$; gray shading), and mean simulated thickness of dense sea ice (blue curve). (**d**) Mean observed MIZ width (black curve), IQR of simulated MIZ width (gray shading), and mean simulated MIZ width (blue curve).

The vertical extent of solid ice (extension of $\psi = 1$ downward from the surface; white shading, Fig. 3a) maximized in spring and minimized in fall, consistent with annual cycles of sea ice thickness estimated from satellite data[47]. The underlying mushy layer ($0 < \psi < 1$; blue shading, Fig. 3a) often extended below sea ice thicknesses based on remote sensing and reanalysis (yellow solid and dashed curves, Fig. 3a), and this occurred mainly at higher latitudes when the lower boundary condition decreased into the mushy temperature range ($T_s < T_b < T_l$). However, the simulated vertical extent of dense ice ($\psi \geq 0.8$) correlated well with sea ice thicknesses obtained from GLORYS2V4, with results from 70°N shown as an example in Fig. 3c.

The model captured the seasonal cycles described above via simulation of heat fluxes and phase changes through the vertical extent of the simulation domain. Some insight into these processes is available by an approximate form of the model equation (2)

$$\rho c \frac{\partial T}{\partial t} - \delta H \frac{\partial \psi}{\partial t} \approx k_z \frac{\partial^2 T}{\partial z^2}, \tag{5}$$

which neglects variations in k_z and uses the fact that $\partial^2 T/\partial z^2$ is orders of magnitude larger than its horizontal counterpart. The right side of (5) is vertical heat flux convergence ($-\partial J_z/\partial z$), and the associated energy is partitioned on the left side into warming and reduction of sea ice concentration, suggesting that positive $\partial^2 T/\partial z^2$ would drive melt conducive to MIZ poleward motion and widening.

Indeed, the rate of change of simulated MIZ location ($\partial \hat{s}/\partial t$) is strongly positively correlated with $\partial^2 T/\partial z^2$ below the ice on the southern flank of the MIZ (Fig. 4a,b). The rate of change of simulated MIZ width ($\partial \hat{w}/\partial t$) is also strongly correlated with $\partial^2 T/\partial z^2$ below the ice, but closer to the central latitude of the MIZ (Fig. 4c,d). The fastest rate of widening aligns well with the largest $\partial^2 T/\partial z^2$, and the timing of the maximum width ($\partial \hat{w}/\partial t = 0$) aligns with the sign reversal of $\partial^2 T/\partial z^2$. Linking back to the observational results, the strong pulse of positive $(T_b - T_0)|_{\phi=s}$ that leads the MIZ widening cycle by three weeks (dotted red curves, Fig. 2d) makes its way into the model interior to provide heat flux convergence below the ice conducive to basal melting and MIZ widening.

Summary and discussion

In observations, the annual cycle of MIZ location tracks the below-ice 273 K isotherm well ($r^2 = 0.97$), and MIZ widening follows the difference between below-ice and skin temperature at a three-week lag $[r^2(w, (T_b - T_0)|_{\phi=s}) = 0.92]$. A moving boundary model adapted to study these cycles as a macroscale phase change front captured 96% of the annual cycle of MIZ location and 78% of the annual cycle of MIZ width. This class of models is usually applied at much smaller scales as one would see in a laboratory setting or sometimes to simulate vertical sea ice growth[48]. In these smaller scale applications, the mushy layer ($T_s < T < T_l$) is a mixture of ice and water; applied at a macroscale, the mushy layer represents a mixed phase region in the vertical and a mixture of ice floes and sea water in the horizontal directions. This model works well though it has no explicit heat advection and no dynamics beyond the rule allowing sea ice to float. Its likelihood of success is bolstered by the signals we found in its observed boundary conditions – the motion of the 273 K isotherm for MIZ position and the strengthening of the vertical temperature gradient for MIZ width. These signals imposed on the boundaries appear to drive the MIZ cycles and have embedded in them an elaborate history of oceanic advective heat fluxes,

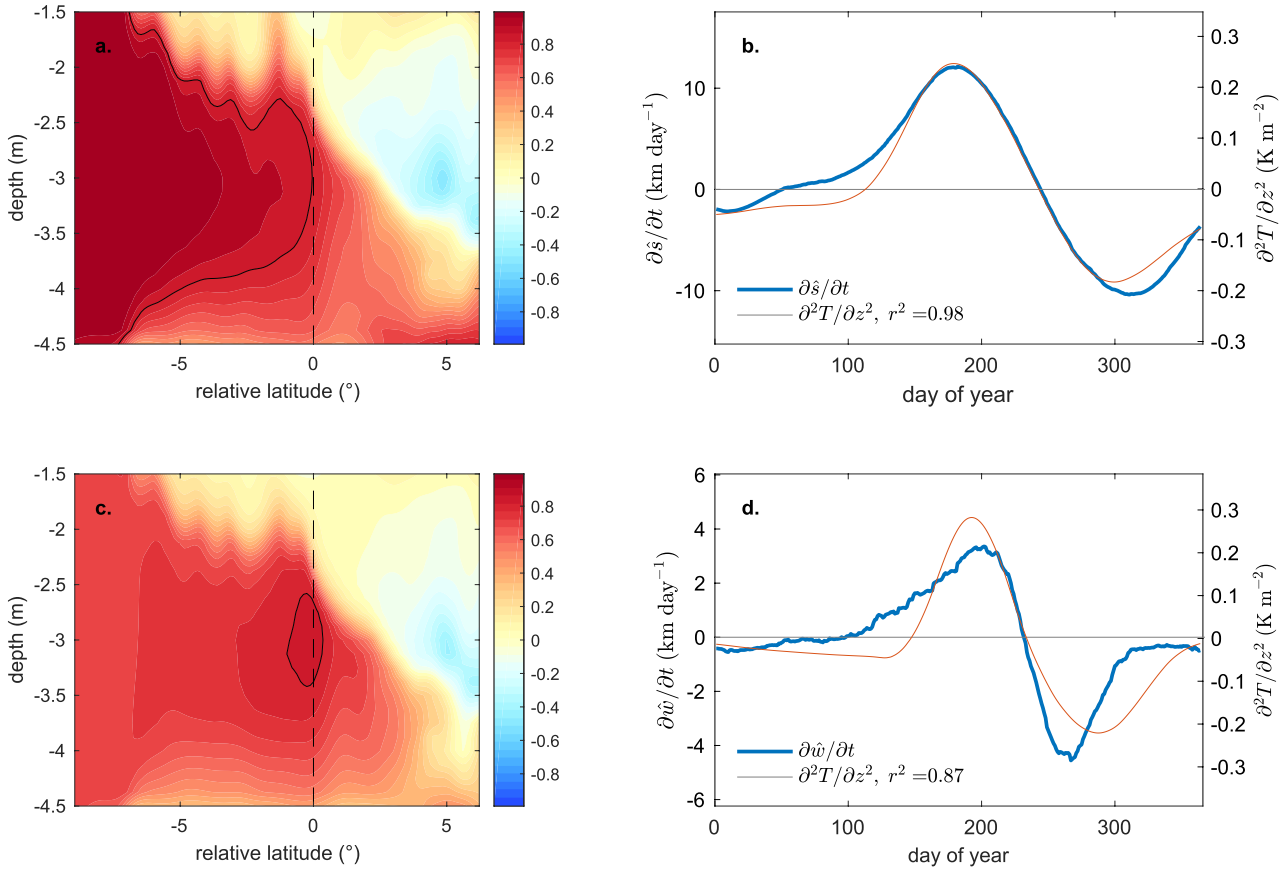

Figure 4. MIZ model derivatives. (**a**) Correlation between $\partial^2 \hat{T}/\partial z^2$ and $\partial \hat{s}/\partial t$. The abscissa is latitude minus the simulated MIZ location ($\phi - \hat{s}$). (**b**) Time series of $\partial^2 \hat{T}/\partial z^2$ averaged within the black contour in panel **a** and $\partial \hat{s}/\partial t$. (**c,d**) Same as **a,b** but for simulated MIZ width $\hat{w}$. A Gaussian filter was used for these calculations, with standard deviations of 14 days on the time coordinate, 0.25° on the latitude coordinate, and 25 cm on the vertical coordinate.

temperature changes on the upper boundary arising from net radiative and turbulent energy fluxes, and possibly also latitudinal gradients in temperature associated with sea ice advection and phase change.

The temperature range of the mushy layer in the model ($T_l - T_s = 0.55$ K) is not large, being two orders of magnitude smaller than the range of temperatures present in the boundary conditions. We took the solid phase threshold (T_s) to be the nominal freezing temperature of sea water ($-1.8\,^\circ$ C) and considered the threshold for the liquid phase as a free parameter. In a region of moderate sea ice concentrations (0.20–0.40) in the MIZ north of Alaska, observed surface temperatures ranged from -1.5 to 1.5°C, with some of this variation interpreted as stemming from proximity to individual floes[49]. The same study reported that surface temperatures in the lower-concentration (0.05) region of the MIZ ranged from 2.3 to 6.1 °C, indicating significant heat storage in the upper ocean. Analysis of monthly gridded sea surface temperature (SST) and sea ice concentration over the Northern Hemisphere indicate a progressive decrease of SST with increasing concentration with more rapid decreases of SST at higher concentrations, and a larger total temperature change across the transition during the warm season (~ 5 °C) than the cold season (~ 3 °C)[50]. The two parameters relating sea ice concentration to temperature in (4) could be allowed to vary over time, perhaps as functions of sea ice thickness or mixed layer depth, but we found that a constant mushy layer definition achieved acceptable correlations and mean absolute errors of MIZ width and location. Further increases in T_l tended to decrease model performance due to a nearly linear increase in the ratio of simulated to observed MIZ width.

While the MIZ is classically described as the portion of the ice pack significantly impacted by ocean wave breakage of the ice into floes[6,8], a thermodynamically-driven MIZ defined precisely by the level curves of the sea ice concentration field is also very useful, particularly for multi-decadal studies of passive microwave satellite data[10,18,37,51]. We note that the National Ice Center also develops operational concentration-based MIZ products[52]. This study focused on multi-year composite seasonal MIZ cycles, but future work is planned to investigate whether the model can capture observed decadal trends in MIZ location and width[10]. It is also of interest to explore how the model results compare to more elaborate models when both are forced by conditions altered by future greenhouse gas concentration scenarios. For these extensions, it may be more convenient to cast the boundary conditions in terms of fluxes, which is a straightforward change to the numerical scheme. More importantly, the drivers of MIZ changes on these longer time scales may differ from the drivers of the seasonal cycles, and work is motivated to determine the extent to which this model can adequately capture such processes.

Methods

Data

For analysis of the observed MIZ, we used the climate data record (CDR) of daily sea ice concentrations at nominally 25-km horizontal resolution based on passive microwave satellite observations, archived by the National Snow and Ice Data Center (NSIDC)[53]. Although algorithms used in the CDR may have greater uncertainty near the ice edge, satellite-based products are widely used in MIZ research and operations because of their superior spatial coverage and continuous measurements[54]. Gridded sea ice thicknesses based on ICESat for spring 2004 were also obtained from NSIDC[55]. For boundary conditions and observational analyses, surface skin temperatures were extracted from the European Centre for Medium-range Weather Forecasts (ECMWF) ERA5 Reanalysis at hourly resolution on a 0.25° grid[56]. We also used daily mean ocean temperatures and sea ice thickness from the Global Ocean Reanalysis and Simulations (GLORYS2V4)[57,58] provided on a 0.25° grid at depth 5.14 m.

MIZ analysis

The concentration-based MIZ was defined as the region of sea ice bounded by $\psi = 0.15$ corresponding to the conventional ice edge[59] and $\psi = 0.80$ corresponding to "close ice" as defined by the World Meteorological Organization[60]. In observations, the width of the MIZ (w) was the arc length of streamlines through the solution to Laplace's equation within the MIZ with boundary conditions $\psi = \{0.15, 0.80\}$ following our prior work[10,11,37]. The location of the MIZ (s) was its area-weighted latitude. To obtain temperatures from the MIZ location, T_b and T_0 were first averaged with respect to longitude over the Bering–Chukchi Sea sector (red outline, Fig. 1). These fields were smoothed using a two-dimensional Gaussian kernel with standard deviations of two weeks and 0.5 degrees of latitude (e.g., yellow contours in Fig. 2b), and then values at $\phi = s$ were obtained via bilinear interpolation in the time-latitude domain.

To analyze the MIZ in the model output, we took the maximum simulated volume fraction of ice in each model column

$$\psi_{max}(t,\phi) = \max_{z_b \le z \le 0} \{\psi(t,\phi,z)\}. \tag{6}$$

The edges of the MIZ at time t were then the first latitudes moving north where ψ_{max} exceeded 0.15 and 0.8. Simulated MIZ location ($\hat{s}$) was the average of these two latitudes, and simulated MIZ width ($\hat{w}$) was their difference converted to kilometers. For the observations and model output, the MIZ width and location were converted to composite daily time series by averaging over each day of year from 2000-2004.

Model parameters

In the mixed phase region, the effective density and effective heat capacity are taken to be concentration-weighted averages

$$\rho = \psi\rho_s + (1-\psi)\rho_l \tag{7}$$

$$c = \psi c_s + (1-\psi)c_l, \tag{8}$$

where subscripts s and l correspond to the solid and liquid phases, respectively. The effective thermal conductivity in the mixed phase region with ice floes and sea water is anisotropic, it differs in the vertical and horizontal directions. We now estimate these key parameters. There is an extensive literature in physics and applied mathematics on the effective or homogenized transport properties of heterogeneous composite media[36,61–63]. The analytic continuation method[61,64–68] provides integral representations as in (9) below for the effective transport coefficients of two-component composites, including[69] electrical and thermal conductivity, complex permittivity, diffusivity, and magnetic permeability. Moreover, all these properties of the same material are coupled to each other through a spectral function in this representation[69,70] and can be indirectly evaluated from measurements of a different parameter. These analytic representations have also been extended to elastic and viscoelastic effective properties[71–74]. These representations distill the complexities of the mixture geometry into the spectral properties of a self-adjoint operator like the Hamiltonian in quantum physics. They yield rigorous bounds on the homogenized transport coefficients, given partial information on the composite geometry, such as the relative area fractions or volume fractions of the components, and whether or not the medium is statistically isotropic or not. For example, the sea ice concentration (SIC) is the satellite-derived area fraction of ocean covered by sea ice.

In the absence of any motion in the liquid phase of the granular two-phase composite of ice floes and sea water, thermal transport is diffusive. In this case, we consider the effective thermal conductivity k^* in any direction, say the vertical z direction, with component conductivities k_s for sea ice and k_l for sea water. Then k^* can be written as[61,64–66]

$$F(u) = 1 - \frac{k^*}{k_l} = \int_0^1 \frac{d\mu(\lambda)}{u-\lambda}, \quad u = \frac{1}{1-k_s/k_l}, \tag{9}$$

where μ is a spectral measure which encodes the composite geometry, with $\int_0^1 d\mu = \psi$. For a discretization of the system, where the self-adjoint operator becomes a matrix, μ can be calculated from the eigenvalues and eigenvectors of the matrix[75,76]. An upper bound on k^* is obtained[66] via a lower bound on F when μ is a Dirac point measure (or Dirac delta function) $\psi\delta_0(\lambda)$ with its mass ψ concentrated at $\lambda = 0$, yielding $F(u) \geq \psi/u$, or $k^* \leq \psi k_s + (1-\psi)k_l$. This upper bound is optimal, in that there are actual composite geometries whose thermal conductivity, as a function of the volume fractions and component parameters, is equal to this arithmetic mean (or concentration-weighted average) expression. Layers aligned vertically are such optimal geometries. If we consider vertically aligned columns whose cross-sections coincide with our given floe geometries, then the vertical thermal conductivity k_z of this composite in 3D is also exactly equal to the arithmetic mean,

$$k_z = \psi k_s + (1-\psi)k_l\,. \tag{10}$$

The lower bound on k^* that corresponds to the upper bound on F in Eq. (9) is obtained through the same procedure, but for $E(u) = 1 - k_s/k^*$, which yields $E(u) \geq \psi/u$, or the the harmonic mean bound, $k^* \geq (\psi/k_s + (1-\psi)/k_l)^{-1}$. This bound is optimal as well, attained by parallel layers aligned perpendicular to the thermal gradient. In this case, though, the horizontal component of the effective thermal conductivity, say k_x, of the granular composite is not in general equal to the harmonic mean, but is reasonably well approximated by it, particularly for matrix-particle geometries[67,68,77], with separated ice floes in a sea water host. Thus as an approximation we take

$$k_x = \left(\frac{\psi}{k_s} + \frac{1-\psi}{k_l}\right)^{-1}. \tag{11}$$

As in the real sea ice system, heat is transported by advection as well as diffusion, we consider advection diffusion processes[41–43]. The analytic continuation method, as formulated by Golden and Papanicolaou[66], which provides Stieltjes integral representations for the homogenized parameter, has been extended to the effective thermal diffusivity D^* (in some direction) of advection diffusion processes[41,44,45]. Rigorous bounds on D^* are obtained given the local diffusivities and information on the geometry of the incompressible velocity field. This theory is more involved than the classical two-component analytic continuation method we used above, and will be explored further in the future.

Since shear-driven mixing dominates over pure thermal diffusion in the oceanic mixed layer, to model the advective contribution to the homogenized diffusivity, we replaced the nominal thermal conductivity of sea water ($0.563\ \mathrm{W\,m^{-1}K^{-1}}$)[78] in Eqs. (10) and (11) with an effective value to account for this mixing,

$$k_l = \rho_l c_l D_T. \tag{12}$$

Here D_T is the effective thermal diffusivity resulting from advective forcing as well as diffusion. Observationally estimated thermal diffusivities span several orders of magnitude in the Arctic[79] (10^{-7}–$10^{-4}\ \mathrm{m^2s^{-1}}$). To determine appropriate values for D_T and the parameters of the concentration function (4), we performed trial simulations spanning the parameter space

$$\begin{aligned} 5\times10^{-7} \leq D_T &\leq 10^{-4}\ \mathrm{W\,m^{-1}\,K^{-1}} \\ 271.4 \leq T_l &\leq 273.0\ \mathrm{K} \\ 0.2 \leq \alpha &\leq 1.4. \end{aligned}$$

The values given in Table 1 were selected to achieve a reasonable seasonal cycle of MIZ location, MIZ width, and sea ice thickness.

Numerical methods

The simulation was performed for the six-year period 1999–2004 with a 24-hour time step, discarding the first year as spinup. We discretized (2) using a fully implicit (backward Euler) time integration scheme[46]. As a two-dimensional model, we considered a MIZ which was radially symmetric about the pole (zero variation in the longitude direction) over the Bering–Chukchi Sea sector, where the latter was defined as the region between the red meridians in Fig. 1 (166°E and 159°W). The model domain spanned the latitude range $50 \leq \phi \leq 90°$N. The vertical extent of the model was set at 5 m so that the lower boundary condition represented a sea-water temperature below the climatological ice thickness in the Bering–Chukchi Sea region[80,81]. The horizontal grid spacing was 1/8° and we used a 12.5-cm vertical grid spacing.

The final term in (2) contains a nonlinearity stemming from the dependence of ψ on T via (4), so T at the current time step was obtained via a constrained iterative scheme. We write the $(m+1)^{\text{th}}$ iteration as

$$a_j T_j^{m+1} = \sum_{\text{nb}} a_{\text{nb}} T_{\text{nb}}^{m+1} + b_j T_j^0 + \delta H_j^0 (\psi_j^{m+1} - \psi_j^0), \tag{13}$$

where the subscript nb indicates the grid points neighboring j. Using a truncated Taylor series expansion[46]

$$\psi_j^{m+1} = \psi_j^m + \frac{df}{dT}[T_j^{m+1} - f^{-1}(g_j^m)], \quad \psi_j^{m+1} \in [0,1] \tag{14}$$

with df/dT evaluated at ψ_j^m. Equation (13) was iterated until δH converged to within 10^{-5}.

A threshold correction was applied to the concentration function (4) enforcing it to take values between 0 and 1. The grid cells with $\psi > 1$ were reset to $\psi = 1$ and gird cells with $\psi < 0$ were reset to $\psi = 0$. In addition, a simple rule was implemented to allow ice to float. In a column, if the surface grid cell(s) were liquid ($\psi = 0$) and had ice ($\psi > 0$) in one or more underlying grid cells, the vertical positions of the surface liquid cell(s) and underlying ice cell(s) were reversed. Without this rule, the ice layer could melt from above and below, leaving an unrealistically submerged ice tongue.

Model boundary and initial conditions

Dirichlet boundary conditions were prepared by averaging daily values with respect to longitude over the Bering–Chukchi Sea region (from 166°E to 210°E, outlined in Fig. 1) over the years 1999–2004. The upper boundary condition at $z = 0$ was defined as the daily mean skin temperature of the ocean or sea ice surface obtained from the ERA5 reanalysis. The lower boundary condition at $z = z_b$ was the below-ice temperature taken at $z = 5$ meter depth from GLORYS2V4. The lateral (depth-dependent) boundary conditions at 50°N and 90°N were prescribed as linear interpolations between T_0 and T_b. For the initial condition, a linear interpolation was made between T_b and T_0 in ice-free columns. Where the GLORYS2V4 initial sea ice thickness (h) was greater than zero on 1 January 1999, T_b was prescribed up the sea water-sea ice interface (i.e., $z_b \leq z < -h$), followed by a linear transition from T_b to T_0 within the sea ice as is typical during the growth season[48].

Data availibility

The GLORYS ocean reanalysis data analyzed here are publicly available from Mercator Ocean International (mercator-ocean.eu), and the sea ice concentration data (Climate Data Record) are pubicly available from NSIDC (nsidc.org). Sea ice concentrations simulated by the model presented here are available from the corresponding author on reasonable request.

Received: 9 November 2023; Accepted: 22 August 2024
Published online: 03 September 2024

References

1. Stroeve, J. C. *et al.* The Arctic's rapidly shrinking sea ice cover: A research synthesis. *Clim. Change* **110**, 1005–1027. https://doi.org/10.1007/s10584-011-0101-1 (2012).
2. Livina, V. N. & Lenton, T. M. A recent tipping point in the Arctic sea-ice cover: Abrupt and persistent increase in the seasonal cycle since 2007. *Cryosphere* **7**, 275–286. https://doi.org/10.5194/tc-7-275-2013 (2013).
3. Stroeve, J. & Notz, D. Changing state of Arctic sea ice across all seasons. *Environ. Res. Lett.* **13**, 103001. https://doi.org/10.1088/1748-9326/aade56 (2018).
4. Parkinson, C. L. & DiGirolamo, N. E. Sea ice extents continue to set new records: Arctic, Antarctic, and global results. *Remote Sens. Environ.* **267**, 112753. https://doi.org/10.1016/j.rse.2021.112753 (2021).
5. Squire, V. A. The marginal ice zone. In *Physics of Ice-covered Seas* (ed. Lepparanta, M.) 381–446 (Helsinki University Printing House, 1998).
6. Wadhams, P. *Ice in the Ocean* (Gordon and Breach Science Publishers, 2000).
7. Squire, V. Of ocean waves and sea-ice revisited. *Cold Reg. Sci. Technol.* **49**, 110–133. https://doi.org/10.1016/j.coldregions.2007.04.007 (2007).
8. Weeks, W. F. *On Sea Ice* (University of Alaska Press, 2010).
9. Barber, D. G. *et al.* Selected physical, biological and biogeochemical implications of a rapidly changing Arctic marginal ice zone. *Progr. Oceanogr.* **139**, 122–150. https://doi.org/10.1016/j.pocean.2015.09.003 (2015).
10. Strong, C. & Rigor, I. G. Arctic marginal ice zone trending wider in summer and narrower in winter. *Geophys. Res. Lett.* **40**, 4864–4868. https://doi.org/10.1002/grl.50928 (2013).
11. Strong, C., Foster, D., Cherkaev, E., Eisenman, I. & Golden, K. M. On the definition of marginal ice zone width. *J. Atmos. Oceanic Tech.* **34**, 1565–1584. https://doi.org/10.1175/JTECH-D-16-0171.1 (2017).

12. Aksenov, Y. *et al.* On the future navigability of Arctic sea routes: High-resolution projections of the Arctic Ocean and sea ice. *Mar. Policy* **75**, 300–317. https://doi.org/10.1016/j.marpol.2015.12.027 (2017).
13. Rolph, R. J., Feltham, D. L. & Schröder, D. Changes of the Arctic marginal ice zone during the satellite era. *Cryosphere* **14**, 1971–1984. https://doi.org/10.5194/tc-14-1971-2020 (2020).
14. Zippel, S. & Thomson, J. Air-sea interactions in the marginal ice zone. *Elementa Sci. Anthr.* **4**, 000095 (2016).
15. Ribic, C. A., Ainley, D. G. & Fraser, W. Habitat selection by marine mammals in the marginal ice zone. *Antarct. Sci.* **3**, 181–186. https://doi.org/10.1017/S0954102091000214 (1991).
16. Perrette, M., Yool, A., Quartly, G. D. & Popova, E. E. Near-ubiquity of ice-edge blooms in the Arctic. *Biogeosci. Discuss.* **7**, 8123–8142. https://doi.org/10.5194/bgd-7-8123-2010 (2010).
17. Post, E. *et al.* Ecological consequences of sea-ice decline. *Science* **341**, 519–524. https://doi.org/10.1126/science.1235225 (2013).
18. Williams, R. *et al.* Counting whales in a challenging, changing environment. *Sci. Rep.* **4**, 4170. https://doi.org/10.1038/srep04170 (2014).
19. Lowry, K. E., van Dijken, G. L. & Arrigo, K. R. Evidence of under-ice phytoplankton blooms in the Chukchi Sea from 1998 to 2012. *Deep Sea Res. Part II* **105**, 105–117. https://doi.org/10.1016/j.dsr2.2014.03.013 (2014).
20. Stephenson, S. R., Smith, L. C. & Agnew, J. A. Divergent long-term trajectories of human access to the Arctic. *Nat. Clim. Change* **1**, 156–160 (2011).
21. Schmale, J., Lisowska, M. & Smieszek, M. Future Arctic research: Integrative approaches to scientific and methodological challenges. *EOS Trans. Am. Geophys. Union* **94**, 292–292. https://doi.org/10.1002/2013EO330004 (2013).
22. Rogers, T. S., Walsh, J. E., Rupp, T. S., Brigham, L. W. & Sfraga, M. Future Arctic marine access: Analysis and evaluation of observations, models, and projections of sea ice. *Cryosphere* **7**, 321–332. https://doi.org/10.5194/tc-7-321-2013 (2013).
23. Thomson, J. & Rogers, W. E. Swell and sea in the emerging Arctic Ocean. *Geophys. Res. Lett.* **41**, 3136–3140. https://doi.org/10.1002/2014GL059983 (2014).
24. Bennetts, L. G., Bitz, C. M., Feltham, D. L., Kohout, A. L. & Meylan, M. H. Marginal ice zone dynamics: Future research perspectives and pathways. *Philos. Trans. R. Soc. A: Math. Phys. Eng. Sci.* **380**, 20210267. https://doi.org/10.1098/rsta.2021.0267 (2022).
25. Horvat, C. Marginal ice zone fraction benchmarks sea ice and climate model skill. *Nat. Commun.* **12**, 2221. https://doi.org/10.1038/s41467-021-22004-7 (2021).
26. Banwell, A. F., Burton, J. C., Cenedes, C., Golden, K. & Åström, J. Physics of the cryosphere. *Nat. Rev. Phys.* **5**, 446–449 (2023).
27. Crank, J. *Free and moving boundary problems* (Oxford science publications, 1987).
28. Kim, C.-J. & Kaviany, M. A numerical method for phase-change problems. *Int. J. Heat Mass Transf.* **33**, 2721–2734. https://doi.org/10.1016/0017-9310(90)90206-A (1990).
29. Hu, H. & Argyropoulos, S. A. Mathematical modelling of solidification and melting: A review. *Modell. Simul. Mater. Sci. Eng.* **4**, 371 (1996).
30. Idelsohn, S. R., Storti, M. A. & Crivelli, L. A. Numerical methods in phase-change problems. *Archiv. Comput. Methods Eng.* **1**, 49–74. https://doi.org/10.1007/BF02736180 (1994).
31. Grandi, D. A phase field approach to solidification and solute separation in water solutions. *Z. Angew. Math. Phys.* **64**, 1611–1624. https://doi.org/10.1007/s00033-013-0301-9 (2013).
32. Wettlaufer, J. S., Worster, M. G. & Huppert, H. E. Natural convection during solidification of an alloy from above with application to the evolution of sea ice. *J. Fluid Mech.* **344**, 291–316 (1997).
33. Worster, M. G. & Wettlaufer, J. S. Natural convection, solute trapping, and channel formation during solidification of salt water. *J. Phys. Chem. B* **101**, 6137–6141 (1997).
34. Feltham, D. L., Untersteiner, N., Wettlaufer, J. S. & Worster, M. G. Sea ice is a mushy layer. *Geophys. Res. Lett.***33**, https://doi.org/10.1029/2006GL026290 (2006).
35. Wells, A. J., Hitchen, J. R. & Parkinson, J. R. G. Mushy-layer growth and convection, with application to sea ice. *Phil. Trans. R. Soc. A* **377**, 20180165 (2019).
36. Golden, K. M. *et al.* Modeling sea ice. *Notices Am. Math. Soc.* **67**, 1535–1555 (2020).
37. Strong, C. Atmospheric influence on Arctic marginal ice zone position and width in the Atlantic sector, February-April 1979–2010. *Clim. Dyn.* **39**, 3091–3102. https://doi.org/10.1007/s00382-012-1356-6 (2012).
38. Luo, B. & Minnett, P. J. Evaluation of the ERA5 sea surface skin temperature with remotely-sensed shipborne marine-atmospheric emitted radiance interferometer data. *Remote Sens.* **12**, 1873. https://doi.org/10.3390/rs12111873 (2020).
39. Cherkaev, E. & Golden, K. M. Inverse bounds for microstructural parameters of a composite media derived from complex permittivity measurements. *Waves Random Med.* **8**, 437–450 (1998).
40. Voller, V. R., Swaminathan, C. R. & Thomas, B. G. Fixed grid techniques for phase change problems: A review. *Int. J. Numer. Meth. Eng.* **30**, 875–898. https://doi.org/10.1002/nme.1620300419 (1990).
41. Avellaneda, M. & Majda, A. Stieltjes integral representation and effective diffusivity bounds for turbulent transport. *Phys. Rev. Lett.* **62**, 753–755 (1989).
42. Fannjiang, A. & Papanicolaou, G. Convection-enhanced diffusion for random flows. *J. Stat. Phys.* **88**, 1033–1076 (1997).
43. Pavliotis, G. A. *Homogenization theory for advection-diffusion equations with mean flow*. Ph.D. thesis, Rensselaer Polytechnic Institute Troy, New York (2002).
44. Murphy, N. B., Cherkaev, E., Zhu, J., Xin, J. & Golden, K. M. Spectral analysis and computation for homogenization of advection diffusion processes in steady flows. *J. Math. Phys.* **61**, 013102 (2020).
45. Murphy, N. B., Cherkaev, E., Xin, J., Zhu, J. & Golden, K. M. Spectral analysis and computation of effective diffusivities in space-time periodic incompressible flows. *Ann. Math. Sci. Appl.* **2**, 3–66 (2017).
46. Voller, V. R. & Swaminathan, C. R. General source-based method for solidification phase change. *Numer. Heat Transf. Part B: Fundam.* **19**, 175–189. https://doi.org/10.1080/10407799108944962 (1991).
47. Kwok, R. & Cunningham, G. F. Variability of Arctic sea ice thickness and volume from CryoSat-2. *Philos. Trans. R. Soc. A: Math. Phys. Eng. Sci.* **373**, 20140157 (2015).
48. Petrich, C. & Eicken, H. *Overview of sea ice growth and properties* 1–41 (John Wiley & Sons, 2017).
49. Bradley, A. C., Palo, S., LoDolce, G., Weibel, D. & Lawrence, D. Air-deployed microbuoy measurement of temperatures in the marginal ice zone upper ocean during the mizopex campaign. *J. Atmos. Oceanic Technol.* **32**, 1058–1070 (2015).
50. Rayner, N. A. *et al.* Global analyses of sea surface temperature, sea ice, and night marine air temperature since the late nineteenth century. *J. Geophys. Res.* **108**, 4407 (2003).
51. Stroeve, J. C., Jenouvrier, S., Campbell, G. G., Barbraud, C. & Delord, K. Mapping and assessing variability in the Antarctic marginal ice zone, pack ice and coastal polynyas in two sea ice algorithms with implications on breeding success of snow petrels. *Cryosphere* **10**, 1823–1843. https://doi.org/10.5194/tc-10-1823-2016 (2016).
52. NIC. National Ice Center products on demand, Accessed June 2016, http://www.natice.noaa.gov (2016).
53. Meier, W. *et al.* NOAA/NSIDC Climate Data Record of Passive Microwave Sea Ice Concentration. Downloaded from http://nsidc.org, Boulder, Colorado USA: National Snow and Ice Data Center. Digital media (2011).
54. Peng, G., Meier, W. N., Scott, D. J. & Savoie, M. H. A long-term and reproducible passive microwave sea ice concentration data record for climate studies and monitoring. *Earth Syst. Sci. Data* **5**, 311–318. https://doi.org/10.5194/essd-5-311-2013 (2013).
55. Stroeve, J. & Meier., W. N. Gridded observational sea ice thickness products, version 1 (2016).
56. Hersbach, H. *et al.* The ERA5 global reanalysis. *Q. J. R. Meteorol. Soc.* **146**, 1999–2049. https://doi.org/10.1002/qj.3803 (2020).

57. Ferry, N. *et al.* GLORYS2V1 global ocean reanalysis of the altimetric era (1992-2009) at meso scale. *Mercator Ocean Q Newslett* (2012).
58. Garric, G. & Parent, L. Quality information document for global ocean reanalysis products. Accessed May 2024. https://catalogue.marine.copernicus.eu/documents/QUID/CMEMS-GLO-QUID-001-025.pdf (2017).
59. Comiso, J. C. Abrupt decline in Arctic winter sea ice cover. *Geophys. Res. Lett.***33**https://doi.org/10.1029/2006GL027341 **(2006).**
60. WMO. *World Meteorological Organization sea-ice nomenclature, terminology, codes and illustrated glossary, WMO/DMM/BMO 259-TP-145* (Secretariat of the World Meteorological Organization, 1985).
61. Milton, G. W. *Theory of Composites* (Cambridge University Press, 2002).
62. Torquato, S. *Random Heterogeneous Materials: Microstructure and Macroscopic Properties* (Springer-Verlag, 2002).
63. Golden, K. M. Climate change and the mathematics of transport in sea ice. *Notices Am. Math. Soc.* **56**, 562–584 (2009).
64. Bergman, D. J. Exactly solvable microscopic geometries and rigorous bounds for the complex dielectric constant of a two-component composite material. *Phys. Rev. Lett.* **44**, 1285–1287 (1980).
65. Milton, G. W. Bounds on the complex dielectric constant of a composite material. *Appl. Phys. Lett.* **37**, 300–302 (1980).
66. Golden, K. & Papanicolaou, G. Bounds for effective parameters of heterogeneous media by analytic continuation. *Comm. Math. Phys.* **90**, 473–491 (1983).
67. Bruno, O. The effective conductivity of strongly heterogeneous composites. *Proc. R. Soc. London A* **433**, 353–381 (1991).
68. Golden, K. M. The interaction of microwaves with sea ice. In *Wave Propagation in Complex Media, IMA Volumes in Mathematics and Its Applications, 75–94* (ed. Papanicolaou, G.) (Springer -Verlag, 1997).
69. Cherkaev, E. Inverse homogenization for evaluation of effective properties of a mixture. *Inverse Prob.* **17**, 1203–1218 (2001).
70. Cherkaev, E. & Zhang, D. Coupling of the effective properties of a random mixture through the reconstructed spectral representation. *Phys. B* **338**, 16–23 (2003).
71. Kantor, Y. & Bergman, D. J. Elastostatic resonances- a new approach to the calculation of the effective elastic constants of composites. *J. Mech. Phys. Solids* **30**, 335–376 (1982).
72. Ou, M. & Cherkaev, E. On the integral representation formula for a two-component composite. *Math. Methods Appl. Sci.* **29**, 655–664 (2006).
73. Cherkaev, E. & Bonifasi-Lista, C. Characterization of structure and properties of bone by spectral measure method. *J. Biomech.* **44**, 345–351 (2011).
74. Cherkaev, E. Internal friction and the Stieltjes analytic representation of the effective properties of two-dimensional viscoelastic composites. *Arch. Appl. Mech.* **89**, 591–607 (2019).
75. Murphy, N. B., Cherkaev, E., Hohenegger, C. & Golden, K. M. Spectral measure computations for composite materials. *Commun. Math. Sci.* **13**, 825–862 (2015).
76. Murphy, N. B., Cherkaev, E. & Golden, K. M. Anderson transition for classical transport in composite materials. *J. Phys. Rev. Lett.* **118**, 036401. https://doi.org/10.1103/PhysRevLett.118.036401 (2017).
77. Orum, C., Cherkaev, E. & Golden, K. M. Recovery of inclusion separations in strongly heterogeneous composites from effective property measurements. *Proc. Roy. Soc. London A* **468**, 784–809 (2012).
78. Sharqawy, M., Lienhard, J. & Zubair, S. Thermophysical properties of seawater: A review of existing correlations and data. *Desalin. Water Treat.* **16**, 354–380. https://doi.org/10.5004/dwt.2010.1079 (2010).
79. Shaw, W. J. & Stanton, T. P. Vertical diffusivity of the Western Arctic Ocean halocline. *J. Geophys. Res.: Oceans* **119**, 5017–5038 (2014).
80. Ricker, R. *et al.* A weekly Arctic sea-ice thickness data record from merged CryoSat-2 and SMOS satellite data. *Cryosphere* **11**, 1607–1623. https://doi.org/10.5194/tc-11-1607-2017 (2017).
81. Wang, X., Key, J., Kwok, R. & Zhang, J. Comparison of Arctic sea ice thickness from satellites, aircraft, and PIOMAS data. *Remote Sens.* **8**, 713. https://doi.org/10.3390/rs8090713 (2016).

Acknowledgements
We are grateful for support from the Applied and Computational Analysis Program at the US Office of Naval Research through grants N00014-18-1-2552 and N00014-21-1-2909. We also gratefully acknowledge support from the Division of Mathematical Sciences at the US National Science Foundation (NSF) through Grants DMS-0940249, DMS-1413454, DMS-2136198, and DMS-2206171.

Author contributions
C.S., E.C., and K.M.G. conceived the model. C.S. performed the experiments and analysed the results. All authors contributed to writing the manuscript.

Competing interests
The authors declare no competing interests.

Additional information
Correspondence and requests for materials should be addressed to C.S.

Reprints and permissions information is available at www.nature.com/reprints.

Publisher's note Springer Nature remains neutral with regard to jurisdictional claims in published maps and institutional affiliations.